



# A review on thermal expansion control in Fe–Ni–Cr austenitic alloys: From Invar effect to advanced power systems

Yian Lin, Pengxin Wang, G.M.A.M. El-Fallah\*

School of Engineering, University of Leicester, Leicester LE1 7RH, UK



## ARTICLE INFO

**Keywords:**  
 Coefficient of thermal expansion (CTE)  
 Fe–Ni–Cr alloys  
 Invar effect  
 Austenitic steels  
 Advanced ultra-supercritical (A-USC) power plants  
 Thermomechanical fatigue

## ABSTRACT

The reliable operation of ultra-supercritical (USC) and advanced ultra-supercritical (A-USC) power plants depends on the performance of thick-walled components under severe thermal and mechanical conditions. Austenitic steels, while offering an attractive balance between cost and high-temperature strength, are constrained by their high coefficient of thermal expansion (CTE), which accelerates thermal fatigue and complicates integration with ferritic components. This review critically evaluates recent advances in the design of low-CTE Fe–Ni–Cr austenitic alloys. Two principal strategies are examined: (1) conventional alloying and precipitation engineering, such as Ni, W, and Mo additions and  $\gamma'$  phase control, to suppress lattice expansion in paramagnetic alloys; and (2) compositional tuning to exploit the Invar effect, particularly through Ni optimisation, to achieve intrinsically low CTE. Key challenges include maintaining high-temperature mechanical integrity, ensuring oxidation resistance, and mitigating CTE mismatch at dissimilar metal joints. Emerging approaches, including Co–Cr balanced designs, Ni/Co ratio optimisation, and high-Al three-phase architectures, demonstrate promising pathways for achieving multi-property optimisation. The review concludes with perspectives on integrating computational thermodynamics and machine learning to accelerate alloy design, enabling simultaneous control of CTE, creep strength, oxidation resistance, and cost for next-generation power plant applications.

## 1. Introduction

Enhancing the efficiency of conventional power generation is essential for reducing fossil fuel consumption and mitigating the environmental impact of combustion [1,2]. Ultra-supercritical (USC) and advanced ultra-supercritical (A-USC) power plants are a key pathway to achieving this goal [3], as higher steam temperatures and pressures directly improve thermal efficiency [4–6]. Typically, USC systems operate at around 620 °C and 30 MPa, while A-USC systems aim for even more demanding conditions of ~700 °C and 35 MPa. Such conditions demand structural materials capable of withstanding prolonged high-temperature loads.

Historically, thick-walled power plant components have been made from ferritic steels. However, their mechanical performance deteriorates significantly above ~600 °C, limiting their long-term application in USC and A-USC environments [7–9]. Austenitic steels provide superior creep resistance and phase stability under these conditions [10]. However, their relatively high coefficient of thermal expansion (CTE) and low thermal conductivity produce steep temperature gradients in thick

sections, which intensify thermal cycling, elevate the risk of thermal fatigue, and shorten component service life. A notable case is the failure of the main steam pipe in the Eddystone Unit 1 power station, where operating conditions had to be downgraded following creep-fatigue damage in 316 stainless steel and dissimilar metal welds [11].

Research has therefore focused on mitigating thermal fatigue through microstructural optimisation, adjusting alloy composition [12], refining grain size [13], and tailoring precipitate distribution [14]. While such strategies improve creep and fatigue resistance, they do not fundamentally overcome the intrinsic challenges of high CTE and mismatch with ferritic steels. A more robust solution lies in designing alloys with inherently lower CTE, thereby reducing thermally induced strain and improving both bulk and interfacial stability during cyclic thermal operation.

This review highlights recent progress in controlling CTE in austenitic alloys. It discusses theoretical foundations, alloy design strategies, performance optimisation approaches, and practical achievements, with emphasis on their application to USC and A-USC power plants. Limitations of current approaches and emerging directions, including the

\* Corresponding author.

E-mail address: [gmae2@leicester.ac.uk](mailto:gmae2@leicester.ac.uk) (G.M.A.M. El-Fallah).

integration of computational modelling and data-driven methods, are also discussed.

## 2. Current challenges and future directions

Structural materials in power plant components are broadly classified into ferritic/martensitic steels, austenitic steels, and nickel-based superalloys (Fig. 1). Ferritic steels dominate in subcritical and supercritical systems, but increasing temperature and steam pressure demand in USC and A-USC plants require a shift toward austenitic steels and Ni-based superalloys to ensure long-term mechanical reliability.

### 2.1. Ferritic steels

Ferritic steels are widely applied in components operating below ~600 °C, such as main steam pipes, reheat headers, and superheaters, due to their favourable combination of tensile and creep strength [16, 17], oxidation and corrosion resistance [18–21], high thermal conductivity, low CTE, and cost-effectiveness [22,23]. As shown in Fig. 2, while some ferritic steels achieve acceptable creep performance at ~600 °C, commercial grades including P92, P122, T91, T92, and 12Cr variants typically have maximum allowable operating temperatures below 620 °C [9].

This temperature limitation is rooted in the body-centred cubic (BCC) crystal structure, which has lower atomic packing density and larger interstitial spaces compared with the face-centred cubic (FCC) structure of austenitic steels. These characteristics lower the activation energy for diffusion, facilitating dislocation climb and accelerating creep deformation at elevated temperatures [24–28]. Enhanced diffusion also promotes carbide coarsening [29–31] and microstructural instabilities such as Z-phase formation [32]. Coarsening of  $M_{23}C_6$  carbides reduces dislocation and grain boundary pinning, while Cr depletion in the surrounding matrix weakens oxidation and corrosion resistance [33]. Suzuki et al. showed that in modified 9Cr–1Mo steels, Z-phase formation coincided with the dissolution of Nb-rich MX carbonitrides, leading to a sudden drop in creep strength [34,35].

Efforts to enhance creep resistance have focused on alloying and processing: Nb and Ti additions stabilise MX carbonitrides [36,37]; W promotes fine Laves phases [38]; Co refines  $M_{23}C_6$  carbides [39]; Ni stabilises NiAl-type phases [40–42]; and optimised C and N contents form nanoscale carbonitrides [43]. B additions retard carbide coarsening and strengthen grain boundaries [44]. Beyond composition, heat treatment [45] and oxide dispersion strengthening [46] have been

explored. Nonetheless, the intrinsic limitations of the BCC structure constrain long-term performance, and service reliability beyond 10<sup>5</sup> h under USC and A-USC conditions remains unproven.

### 2.2. Austenitic steels

Austenitic steels offer superior creep resistance, more stable grain boundaries, and improved oxidation and corrosion resistance [47]. Their development has relied on systematic alloying, particularly increasing Ni and Cr content to stabilise the FCC phase, enhance solid-solution strength, and improve corrosion resistance (Fig. 3) [48]. However, detailed roles of individual elements are covered in other reviews [46,49].

The FCC structure also supports stable carbides, nitrides, and other strengthening phases, which remain effective at elevated temperatures [46]. These precipitates inhibit dislocation motion and grain boundary sliding, while resisting coarsening or transformation into detrimental phases. However, FCC alloys inherently possess high CTE due to shorter interatomic bond lengths and higher bond energies, and their dense packing reduces electron mobility, resulting in low thermal conductivity [50]. As summarised in Table 1, austenitic steels thus combine high CTE with poor thermal conductivity, compared with ferritic steels and Ni-based alloys, making them more susceptible to thermal fatigue under cyclic loading. Thermal cycling from start-up/shut-down, load fluctuations, and internal gradients induces stresses proportional to both CTE and the magnitude of the gradient. These stresses accumulate in thick sections and at dissimilar-metal junctions, where CTE mismatch with ferritic steels accelerates crack initiation and propagation [51].

### 2.3. Nickel-based superalloys

Nickel-based superalloys have been introduced into critical components to further extend service life under extreme conditions. As illustrated in Fig. 4, they provide the highest creep rupture strength at a given temperature, surpassing both austenitic and ferritic steels [52]. However, cost becomes a decisive factor when comparing material options for large-scale applications. Fig. 5 highlights that, even at comparable performance, their cost substantially exceeds that of high-Cr, high-Ni austenitic steels [53]. In addition, their residual CTE mismatch with ferritic steels and limited processability and weldability present further barriers to large-scale deployment [54]. For this reason, Ni-based alloys are generally reserved for the most demanding components, such as rotors and turbine blades, where performance outweighs economic considerations.

Overall, FCC-based alloys represent the most viable route for high-temperature power generation applications. Optimising austenitic steels to retain their inherent creep resistance while reducing thermal expansion offers a promising pathway to balance cost, performance, and compatibility. Such advances would support broader deployment of USC and A-USC technologies, enabling further improvements in efficiency and long-term reliability.

## 3. Conventional strategies for reducing the CTE in austenitic alloys

CTE in metallic alloys is closely linked to bond strength. For a fixed crystal structure, modifying the electronic environment through alloying alters the bond stiffness and, consequently, the thermal expansion. In austenitic alloys, the principal elements, Fe, Ni, and Cr, not only stabilise the FCC structure but also strongly influence CTE. Their effects are discussed below, followed by those of minor alloying elements, lattice constant considerations, and secondary phases.

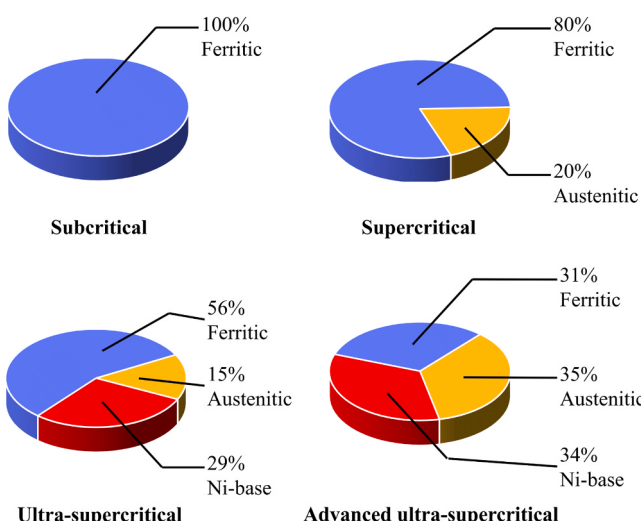


**Fig. 1.** Ratio between ferritic, austenitic, and Ni-based materials in different power plants, data from [15].

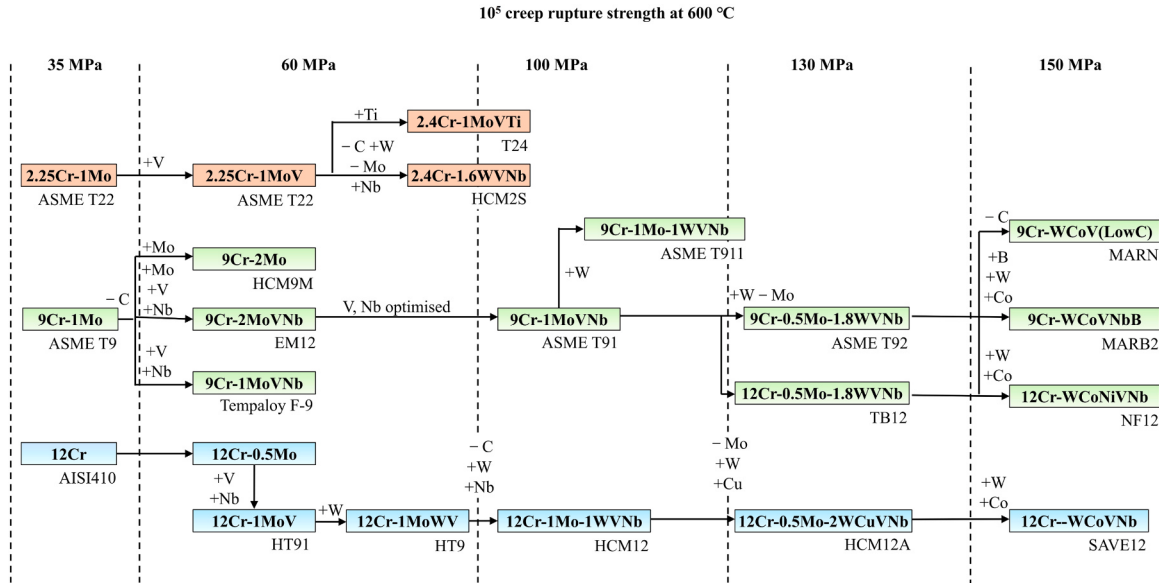


**Fig. 2.** Evolution of ferritic steel compositions and associated creep performance improvements.

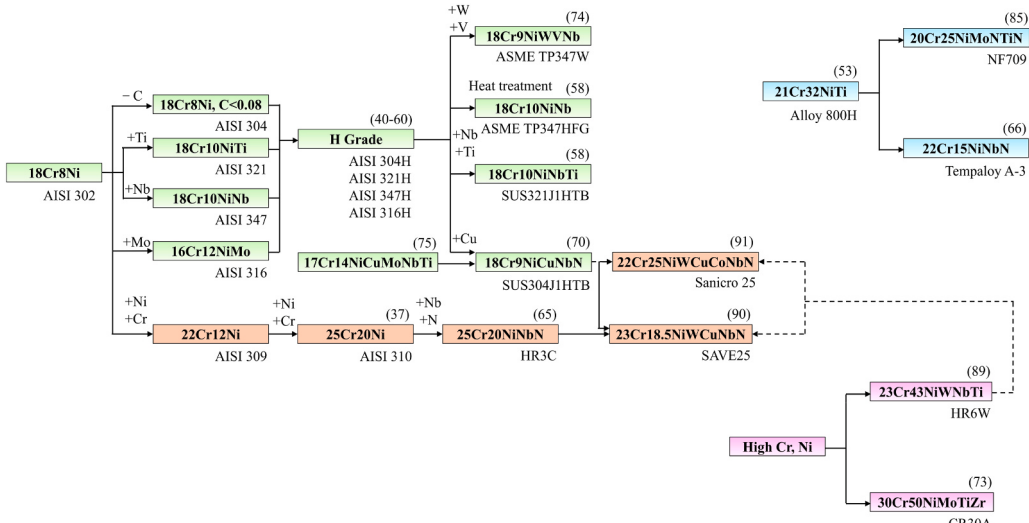


**Fig. 3.** Development progress of austenitic steels, the numbers in parentheses indicate the creep rupture strength at 700 °C for 100,000 h, after Masuyama [48].

**Table 1**

Thermal conductivity and CTE of ferritic, austenitic, and Ni-based alloys used in power plants, data from [55].

Material type	Thermal conductivity (W/m °C)	CTE ( $\times 10^{-6}$ °C $^{-1}$ )
Ferritic steel	~50	~11
Austenitic steel	~16	~18
Ni-based alloy	~24	~14.7

### 3.1. Role of principal elements

Ni is the most effective element for reducing CTE in Fe-Ni-Cr alloys. As shown in Fig. 6, the CTE of austenitic steels generally decreases with increasing Ni content. The mechanism lies in electronic band structure modification: additional Ni electrons occupy states near the Fermi level, strengthening metallic bonds, raising the Debye temperature, and thereby lowering CTE through the Grüneisen relation [56]. This also explains why Ni-based superalloys typically exhibit lower CTE than

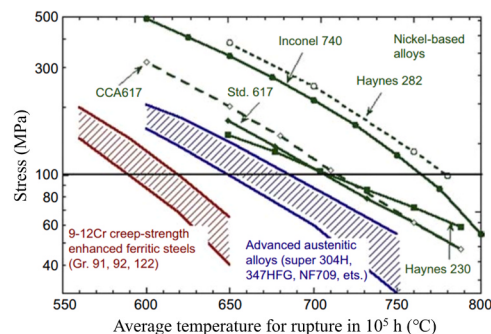


**Fig. 4.** 100,000 h creep rupture strength as a function of temperature for ferritic, austenitic, and Ni-based alloys [52].

Fe-based austenitic steels.

By contrast, Fe additions increase CTE. Hull et al. [59] reported that paramagnetic alloys  $\text{Fe} > (\text{Ni} + \text{Co})$  have higher CTE than those with

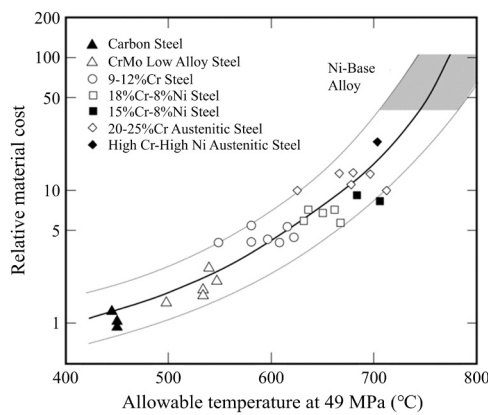


**Fig. 5.** Relation between allowable metal temperature at 49 MPa stress and relative material cost for different classes of steels and Ni-based alloys. Ferritic steels (carbon steels, CrMo steels, and 9–12 % Cr steels) dominate the low-temperature, low-cost region; austenitic steels occupy the intermediate range; Ni-based alloys achieve the highest temperatures but at significantly higher cost [53].

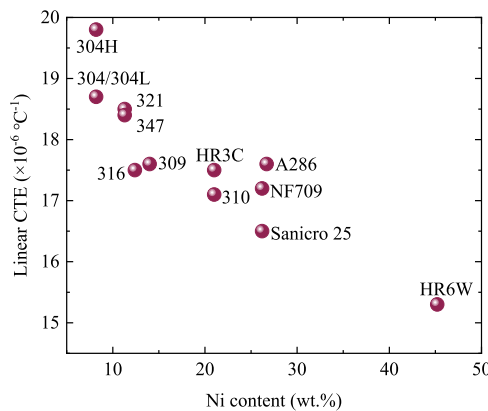


**Fig. 6.** CTE of selected austenitic steels as a function of the Ni content, data from [53,57,58].

$\text{Fe} < (\text{Ni} + \text{Co})$ , a result later confirmed by Wu et al. [60] (Table 2, Fig. 7). Increasing Fe content increases the fraction of weaker Fe–Fe bonds compared with Ni–Ni bonds, reducing lattice rigidity and resulting in a larger thermal expansion.

Cr has a more complex role; most studies indicate Cr increases CTE in both Fe- and Ni-based alloys [51,60–62]. However, at higher concentrations, Cr can promote the precipitation of low-CTE  $\alpha$ –Cr, which lowers expansion. This effect is amplified in Fe-rich systems due to strong magnetic interactions: antiferromagnetic Cr interacts with ferromagnetic Fe, enhancing exchange energy and vibrational anharmonicity, thereby elevating CTE unless  $\alpha$ –Cr precipitation occurs [59].

**Table 2**

Chemical compositions (wt%) of the alloy studied, with the balance being Ni [60].

Type	C	Mo	W	Cr	Fe	Al	Ti
NF1	0.05	2.1	1.9	15	35	1.9	1.3
NF2	0.05	2.1	1.9	12.5	40	1.9	1.3
NF3	0.05	2.1	1.9	15	35	1.0	0.6
N1	0.05	2.1	1.9	25	-	1.9	1.3
N2	0.05	2.1	1.9	15	-	1.9	1.3

### 3.2. Influence of minor alloying elements

Beyond the major constituents, minor alloying elements provide further control over CTE. Hull et al. [59] found that interstitials (C, N) slightly reduce expansion by constraining atomic vibrations within the lattice. While Mo and Si exert stronger reductions. In contrast, Mn markedly increases CTE, with the effect saturating at ~ 8 wt% due to a balance between lattice expansion and local bonding constraints.

W is particularly effective: alloys such as Sanicro 25 (with ~ 3 wt% W) show much lower CTE than W-free NF709 despite similar Ni levels. The HR6W alloy, containing ~ 6 wt% W achieves exceptionally low expansion. The primary reason is that the relatively large W atoms, when dissolved in the  $\gamma$  matrix, increase local lattice constraints and enhance metallic bond rigidity, thereby restricting lattice vibrations and significantly reducing the CTE [63]. A similar effect is observed for other relatively large atoms such as Mo [64]. In addition, both W and Mo improve the creep resistance of the alloy, making them particularly important for optimising thermal expansion behaviour in high-temperature applications. In Ni-based alloys, similar trends are observed: Mn and Co increase CTE, while Nb, Al, Ti, W, and Mo act to suppress it [51,59,61,62,65]. Some reports, however, note that Al and Ti can also raise CTE when dissolved in the  $\gamma$  matrix [60,66].

### 3.3. Interatomic-potential origin of thermal expansion

A general correlation exists between lattice constant and CTE: larger lattice constants often correspond to lower expansion [60,67]. At very short interatomic separations  $x < x_0$ , atoms experience steep repulsive forces; at long separations  $x > x_0$ , attractive forces dominate. At equilibrium spacing ( $x = x_0$ ), atoms vibrate around a potential well. With increasing temperature, the average position shifts toward the shallower attractive side, increasing interatomic distance. Alloys with larger lattice constants exhibit smaller relative shifts, and thus lower CTE.

Fig. 8 schematic comparison of two interatomic potential curves illustrating the origin of thermal expansion. Curve a (red) represents an alloy with a smaller lattice constant  $x_a$ , while curve b (blue) corresponds to an alloy with a larger lattice constant  $x_b > x_a$  and a shallower repulsive slope. As the temperature increases from  $T_0$  to  $T_2$ , the mean interatomic spacing increases from  $x_a$  to  $x'_a$  for curve a, and from  $x_b$  to  $x'_b$  for curve b. The thermal expansion  $\Delta x_a$  is greater than  $\Delta x_b$ , indicating that the alloy with the larger lattice constant exhibits a lower CTE.

This relationship can be quantified as [68]:

$$\alpha = \frac{1}{x_0} \frac{d\langle \Delta x \rangle}{dT} = \frac{3b_2 k_b}{4b_1^2 x_0} \quad (1)$$

where  $k_b$  is Boltzmann's constant and  $b_1, b_2$  are positive constants describing the potential well. Approximating the equilibrium distance as twice the atomic radius ( $x_0 \approx 2r$ ) and using the FCC relation  $r = \frac{\sqrt{2}}{4}a$  between atomic radius and lattice constant  $a$ , Eq. (1) becomes:

$$\alpha = 3\sqrt{2}b_2 k_b / 4b_1^2 a \quad (2)$$

Eq. (2) confirms the inverse relation between lattice constant and CTE in FCC alloys. However, this trend holds only within the same matrix type. In Fe–Cr alloys, where strong Fe–Cr magnetic interactions increase the repulsive exchange energy and enhance the anharmonicity of atomic vibrations, which can override the simple lattice-constant rule. For example, Fe-rich alloy NF3 displays a larger lattice constant than non-ferrous alloy N2 but a higher CTE (Fig. 7).

Beyond first-principles treatments, several groups have applied regression analyses to large alloy databases. For example, Yamamoto et al. derived an empirical relation linking CTE to specific alloying additions [61]. Although such formulas capture qualitative trends, they are system-specific and often valid only over narrow compositional ranges, limiting their predictive power for new alloy families [62,69].

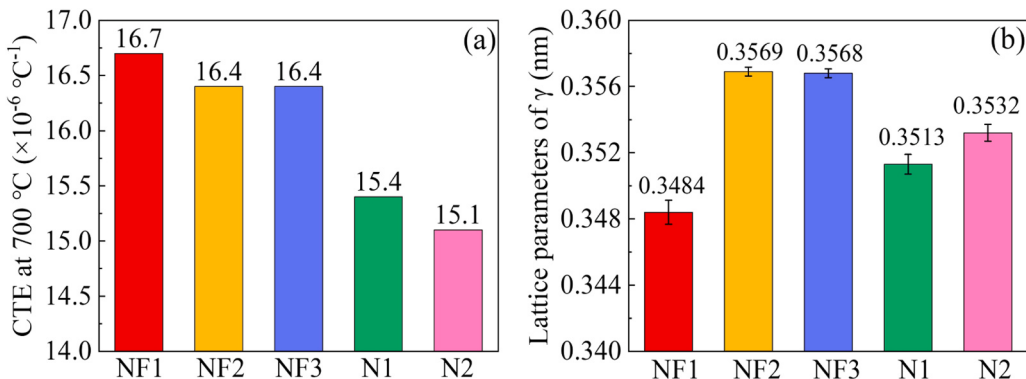


Fig. 7. (a) CTEs of Fe- and Ni-based alloys with different compositions; (b) lattice parameter comparison, after [60].

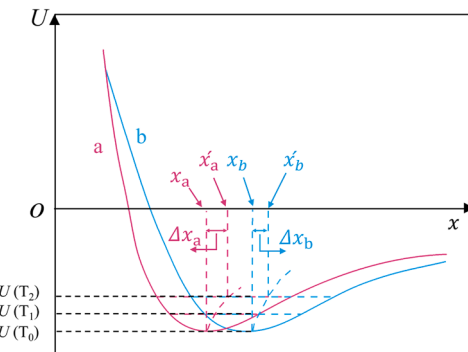


Fig. 8. Schematic of interatomic potential curves illustrating the origin of thermal expansion.

#### 3.4. Effect of secondary phases

In addition to solute effects, secondary phases such as carbides and  $\gamma'$ , which is an ordered  $\text{L1}_2 \text{Ni}_3(\text{Al}, \text{Ti})$  precipitate acting as a strengthening phase, also influence the CTE. Yan et al. [70] measured the CTE of  $\gamma$ ,  $\gamma'$ , and carbides in Ni-based superalloys, finding the order:  $\text{MC} < \text{M}_{23}\text{C}_6 < \gamma' < \gamma$ . Carbides and grain boundary phases occupy limited volume fractions and thus have a negligible overall impact. By contrast,  $\gamma'$  is a major strengthening phase and its fraction significantly affects thermal expansion. The overall CTE of an alloy can be expressed as a weighted sum [71]:

$$\alpha_{\text{total}} = \alpha_{\gamma} V_{\gamma} + \alpha_{\gamma'} V_{\gamma'} \quad (3)$$

where  $V_{\gamma}$  and  $V_{\gamma'}$  are the phase volume fractions. Al and Ti, the key  $\gamma'$ -formers, increase the CTE of the  $\gamma$  matrix by reducing its lattice constant, but  $\gamma'$  itself has a much lower CTE than  $\gamma$ . Thus, the partitioning of Al and Ti between  $\gamma$  and  $\gamma'$  determines the overall behaviour. Some studies have attempted to determine the CTEs of the  $\gamma$  matrix and  $\gamma'$  phase using X-ray diffraction techniques. However, this approach faces significant challenges, as the diffraction peaks of the two phases often overlap, making separation difficult, and at elevated temperatures, the peak intensity and resolution of both phases become considerably weakened [72,73]. Because of these limitations, some researchers have turned to first-principles calculations to evaluate the thermal expansion behaviour of the  $\gamma$  matrix and  $\gamma'$  phase [74–76].

Cheng et al. [77] combined experiments and first-principles calculations to study this effect. They showed that when Al and Ti remain in the  $\gamma$  matrix, CTE rises; when incorporated into  $\gamma'$ , CTE falls (Fig. 9). Increasing Ti lowers both  $\gamma$  and  $\gamma'$  CTEs while stabilising  $\gamma'$  formation. The net effect is a decrease in total expansion, particularly at lower Al/Ti ratios. At high Al and Ti levels, dissolution of  $\gamma'$  above its solvus temperature causes CTE to rise again as these elements re-enter the  $\gamma$  matrix.

#### 3.5. Limitations of conventional approaches

Conventional alloying strategies, adjusting Fe, Ni, Cr, and minor solutes and controlling the  $\gamma/\gamma'$  phase balance, have significantly lowered the CTE of austenitic alloys. Elements such as W and Mo are

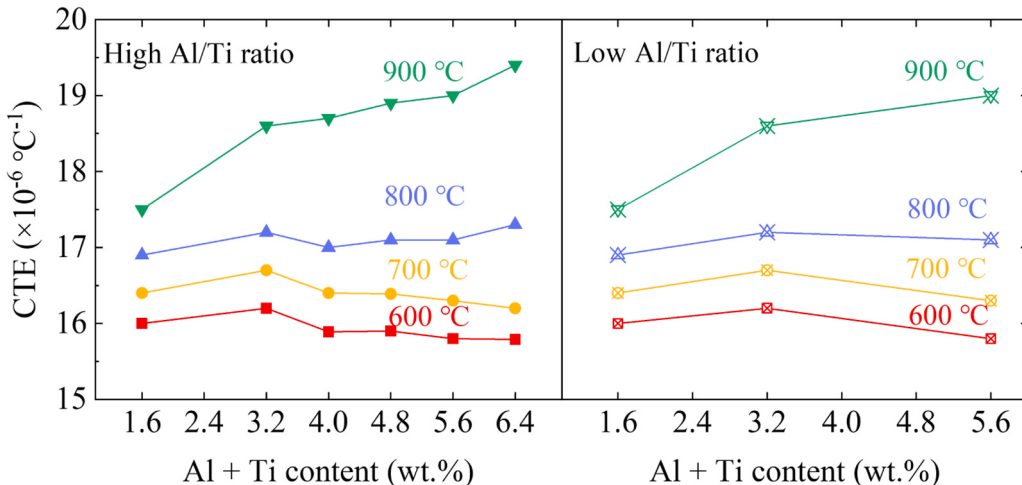


Fig. 9. Effect of Al + Ti content and Al/Ti ratio on the CTE of Fe-Ni-Cr alloys. The low and high Al/Ti ratios are approximately 0.6 and 1.6 (wt%), respectively, after [77].

particularly valuable because they both suppress thermal expansion and enhance creep strength, while Al and Ti promote low-CTE  $\gamma'$  precipitates. However, practical alloy design requires careful trade-offs: excessive Ni further reduces CTE but increases cost; addition of W or Mo may impair workability and processing [78,79]; sufficient Cr must be retained to maintain oxidation and corrosion resistance, even though it can raise CTE; and adequate Fe is needed to manage both cost and mechanical properties. Despite these optimisations, conventional composition-driven approaches exhibit diminishing returns in further reducing the CTE. Even with extreme compositional adjustments, such as the high Ni and low Fe contents used in Ni-based superalloys, the resulting CTE values remain noticeably higher than those of ferritic steels. This persistent mismatch reflects the intrinsic limitation of traditional alloy design strategies, which cannot effectively suppress thermal expansion when the alloys remain fully paramagnetic under service conditions. Therefore, alternative design concepts, particularly those that exploit magnetic effects such as the Invar effect, are required to achieve more substantial CTE reduction and enhance compatibility between austenitic and ferritic components.

#### 4. Reducing CTE by leveraging the Invar effect

Magnetic ordering in austenitic Fe–Ni alloys couples strongly with lattice vibrations, leading to anomalous thermal expansion behaviour. Most austenitic Fe–Ni alloys exhibit CTE values of  $14\text{--}21 \times 10^{-6} \text{ }^{\circ}\text{C}^{-1}$  [80,81]. In 1897, Guillaume discovered Fe–36Ni (later named Invar 36), whose length remains nearly constant with temperature, hence the name *Invar* (invariable) [82,83]. This discovery laid the foundation for designing low-expansion alloys by exploiting magneto-volume effects.

##### 4.1. Mechanistic basis of the Invar effect

Competing models have been proposed to explain the unusually low CTE in Fe–Ni alloys. Weiss's “two- $\gamma$ -state” model attributes the effect to differences in atomic volume between electronic/magnetic states of  $\gamma$ -Fe [84]. Kim et al. later proposed temperature-dependent dipole interactions among Fe–Fe and Fe–Ni pairs, with Ni–Ni interactions largely unaffected due to the low Fe spin-state population [85]. However, Kim's model could not account for “super-Invar” alloys ( $\sim 5$  wt% Co addition) exhibit even lower CTE than Invar 36 [86]. Consequently, Weiss's two- $\gamma$ -state model remains the most widely accepted explanation [87–89].

In Weiss's theory,  $\gamma$ -Fe contains two electronic states:  $\gamma_0$ , which is antiferromagnetic at 0 K with a magnetic moment of  $\sim 0.5 \mu\text{B}$  per atom; and  $\gamma_1$ , which forms when thermal excitation shifts an electron within the d-band, producing a higher-energy ferromagnetic state with a magnetic moment of  $\sim 2.8 \mu\text{B}$  per atom. Assuming that the CTE of each state equals that of ferrite, Kaufman et al. derived the following temperature-volume relationships [90]:

$$V_m^{\gamma_0} = 6.695(1 + 2.043 \times 10^{-5}T + 1.52 \times 10^{-8}T^2) \text{ cm}^3 \text{ mol}^{-1} \quad (4)$$

$$V_m^{\gamma_1} = 7.216(1 + 2.043 \times 10^{-5}T + 1.52 \times 10^{-8}T^2) \text{ cm}^3 \text{ mol}^{-1} \quad (5)$$

$V_m^{\gamma_0}$  and  $V_m^{\gamma_1}$  represent the molar volumes of  $\gamma_0$  and  $\gamma_1$ , respectively. Since  $\gamma_1$  has a larger molar volume, its fraction increases with temperature in low-Ni austenite, boosting thermal expansion relative to ferritic steels, Fig. 10. At constant temperature, external pressure suppresses  $\gamma_1$  in the  $\gamma$  phase [91], while lattice expansion (e.g., depositing austenitic films on heated Cu substrate) can trigger transitions [91].

Sufficient Ni additions make the  $\gamma_1$  state energetically favourable (negative energy gap  $E_1$ ), producing a ferromagnetic ground state, Fig. 11(a). At  $\sim 34.4$  at% Ni, the ground state corresponds to high-volume ferromagnetic  $\gamma_1$  austenite. As the temperature increases below the Curie temperature ( $T_c$ , the temperature above which a ferromagnetic material becomes paramagnetic),  $\gamma_1$  gradually transforms

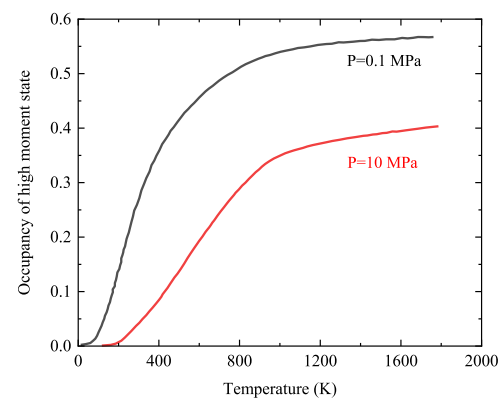


Fig. 10. Relative population of high moment spin states ( $\gamma_1$ ) in  $\gamma$ -Fe as a function of temperature and pressure, after [91].

into the low-volume  $\gamma_0$  phase, compensating for thermal expansion. Conversely, decreasing the temperature reverses the transformation, offsetting contraction. This bidirectional compensation mechanism underpins the Invar effect. Similar low-expansion behaviour occurs in Fe-based alloys containing Pd or Pt [92,93].

##### 4.2. Alloying to raise the Curie temperature

Invar 36 exhibits an exceptionally low CTE between  $-100 \text{ }^{\circ}\text{C}$  and  $100 \text{ }^{\circ}\text{C}$ , making it indispensable for applications requiring precise dimensional stability. It is widely used in precision optical assemblies (such as telescope mirror mounts and interferometer frames), cryogenic storage systems for liquefied natural gas (LNG), where thermal stress control is critical, particularly in connection structures such as supports and sealing flanges, where thermal strain mismatches between interfaces can lead to leakage or structural failure. It is also utilised in laser resonator housings and alignment components that require minimal thermal drift, as well as accelerometer and microelectromechanical system (MEMS) substrates to ensure calibration stability. Additionally, it is used in metrological instruments and precision gauges that rely on consistent geometry under varying thermal conditions [94–96].

In recent years, advances in materials processing and post-treatment have enabled the fabrication of Invar 36-based metamaterials with tunable CTEs. Casting is the most commonly used fabrication route for Invar 36. Rapid solidification variants, such as vacuum arc remelting (VAR), can refine grains and reduce casting defects (e.g., shrinkage and porosity), thereby lowering CTE [97]. Advanced additive manufacturing techniques allow precise control of CTE and mechanical properties through optimised energy input and scanning strategies [98–101], while the unique build direction inherent to these processes can introduce anisotropy, resulting in thermal expansion behaviour distinct from cast samples [102]. Post-treatment processes further influence CTE: cold working introduces dislocations and residual stresses to reduce expansion [103,104]; heat treatment relaxes residual stresses, but excessive temperatures may coarsen grains and slightly increase CTE [102,105]; hot isostatic pressing (HIP), promoting structural stability, reduces internal porosity and slightly increases CTE [106]. Wei et al. [107] proposed two-dimensional structures based on dual-material units using Invar 36, achieving controllable thermal expansion. Subsequent studies extended this concept to three-dimensional architectures, similarly, achieving tunable thermal expansion [108,109]. These studies demonstrate that low-CTE alloys such as Invar 36, when combined with advanced processing and post-treatment techniques, can serve as key constituent materials for constructing metamaterials with customised thermal expansion behaviour. However, its use at elevated temperatures is limited by low mechanical strength and a  $T_c$  of only  $\sim 240 \text{ }^{\circ}\text{C}$  [110]. Above this temperature, Invar 36 becomes fully paramagnetic and loses its low-expansion characteristic. To enable high-temperature service,

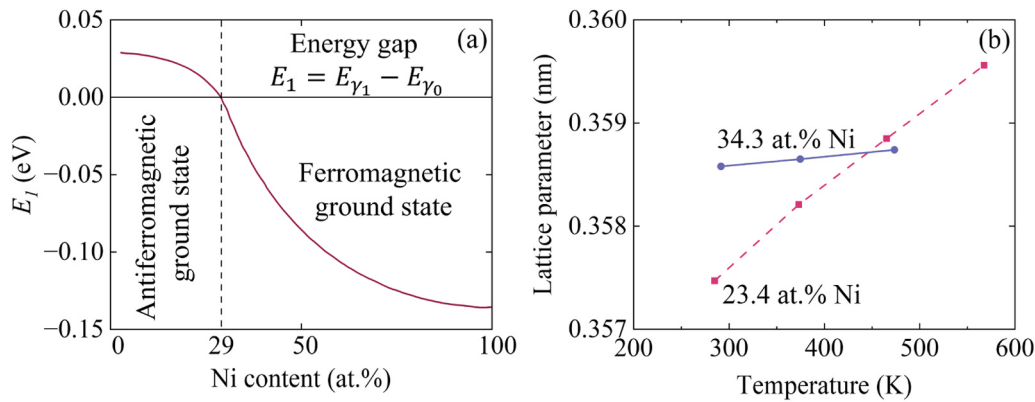


**Fig. 11.** (a) Energy gap  $E_1$ , between  $\gamma$  states of austenite vs Ni concentration; (b) austenite lattice parameters vs Ni (at%) and temperature, after [84,89].

modified or multi-component Invar-type alloys must balance thermal stability with mechanical performance.

Commercial Invar 36 typically contains Si (for castability), Mn (to reduce S segregation), and Cr (for corrosion resistance). Beyond these additions, Solov'eva et al. [111] introduced Ru and Rh into vacuum induction melted (VIM) Invar 36 to achieve a CTE near  $5 \times 10^{-6} \text{ }^{\circ}\text{C}^{-1}$  and extend the effective temperature range. However, these elements had little impact on  $T_c$ , which remained between 230 and 300  $^{\circ}\text{C}$ . Ha and Min [112] explored carbon additions to Mo–Co–Cr-containing Invar 36. Increasing C content improved tensile strength (exceeding 1000 MPa at 0.38 wt% C after hot rolling) with only moderate ductility loss, attributed to carbide dispersion or dissolution. Nevertheless, C additions also raised the CTE ( $4-5 \times 10^{-6} \text{ }^{\circ}\text{C}^{-1}$  below 200  $^{\circ}\text{C}$ ), illustrating the trade-off between strength and dimensional stability.

Tsuda et al. reported that most trace alloying additions increase the CTE of Invar 36, except for Cu, which tends to depress  $T_c$  [113]. Tanji et al. investigated the effect of Ni content on thermal expansion in Fe–Ni alloys at elevated temperatures and found that the Ni composition corresponding to the minimum CTE shifts with temperature, reflecting the temperature-dependent magnetic state of the alloy [114]. As shown in Fig. 12, Fe–Ni alloys with ~40 at% Ni at 200  $^{\circ}\text{C}$  and ~45 at% Ni at 400  $^{\circ}\text{C}$  exhibit CTE values lower than Invar 36, attributable to their magnetic state and its dependence on composition and  $T_c$ .

Introducing Co is an effective strategy to raise the  $T_c$  of Invar-type alloys, thereby extending the temperature range over which the Invar effect operates. Wang et al. examined the influence of composition on CTE in the Fe–Ni–Co system [115]. As shown in Fig. 13, a distinct low-expansion region, attributable to the Invar effect, lies within the

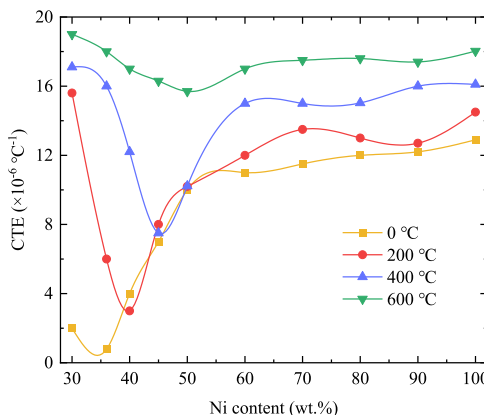


**Fig. 12.** Relationship between Ni content and CTE in Fe–xNi alloys at various temperatures. At each temperature, the CTE decreases and then increases with Ni content, while the minimum shifts to higher Ni levels as temperature rises, after [114].

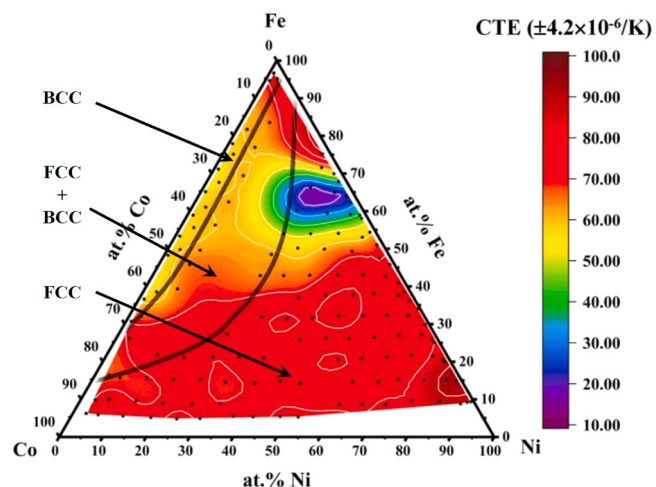


**Fig. 13.** Contour map of volumetric CTEs in the Fe–Ni–Co system (80–200  $^{\circ}\text{C}$ ). The two lines indicate phase boundaries at 700  $^{\circ}\text{C}$  [115].

FCC single-phase field, centred around the compositions of classical Invar (Fe<sub>64</sub>Ni<sub>36</sub>) and super Invar (Fe<sub>63</sub>Ni<sub>32</sub>Co<sub>5</sub>).

As Co content increases, both CTE and  $T_c$  rise, for example, in Fe<sub>54</sub>Ni<sub>36</sub>Co<sub>10</sub>, the CTE increases from  $4.01 \times 10^{-6} \text{ }^{\circ}\text{C}^{-1}$  (Fe<sub>64</sub>Ni<sub>36</sub>) to  $6.54 \times 10^{-6} \text{ }^{\circ}\text{C}^{-1}$ , while  $T_c$  rises from 240  $^{\circ}\text{C}$  to 432  $^{\circ}\text{C}$ . In Fe<sub>45</sub>Ni<sub>45</sub>Co<sub>10</sub>,  $T_c$  further increases to 581  $^{\circ}\text{C}$ , but the CTE sharply rises to  $11.21 \times 10^{-6} \text{ }^{\circ}\text{C}^{-1}$ , indicating that excessive Co compromises the Invar effect. Thus, moderate Co additions are beneficial for improving high-temperature applicability, but maintaining the FCC single-phase region is essential to preserve low thermal expansion. Minor additions (< 5 at%) of Cu, Cr, and Mn do not significantly shift the alloy from the Invar domain, offering flexibility for performance optimisation.

#### 4.3. From Invar-type to controlled thermal expansion alloys

The limitations of low-alloyed Invar-type systems in high-temperature service have driven the development of controlled thermal expansion alloys that combine low CTE with enhanced mechanical strength. These alloys are designed for environments where thermal expansion control remains important but must be balanced with creep resistance, oxidation resistance, and structural integrity.

A critical observation during alloy design was that chromium additions increase CTE and lower the  $T_c$ . As shown in Fig. 14, adding 3.6 wt % Cr to Incoloy 903 increased the CTE by ~10 % beyond the inflection point and reduced lowered  $T_c$  from 406  $^{\circ}\text{C}$  to 330  $^{\circ}\text{C}$  [116]. To overcome this, the Ti-precipitation-strengthened alloy In698 was developed by

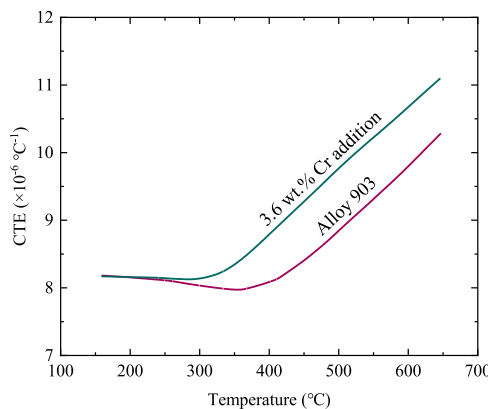


**Fig. 14.** Effect of Cr on the CTE of Incoloy 903, showing that increased CTE and reduced inflection temperature narrow the effective Invar range, after [116].

eliminating Cr and incorporating Ti, achieving controlled thermal expansion between 427 °C and 487 °C. Later, Nb was added to improve thermal stability, slow precipitation hardening, stabilise ageing precipitates, and enhance weldability.

Among the earliest controlled thermal expansion alloys, Incoloy 903 combined precipitation strengthening with the Invar effect to achieve a balance between high-temperature strength and low thermal expansion. The compositions of Incoloy 903 and subsequent alloys reflect a systematic design strategy: high Ni to induce the Invar effect; Cr limited to very low levels; Co to raise  $T_c$  while maintaining low CTE; Nb for solid-solution and precipitation strengthening; and Al and Ti to promote  $\gamma'$ -phase formation. These principles guided the development of Incoloy 907 and 909, as well as advanced systems such as HRA929, HRA929C, THERMO-SPAN, and three-phase alloys, as summarised in Table 3.

Despite these advances, Incoloy 903 remained vulnerable to stress-accelerated grain boundary oxidation (SAGBO), which promotes notch embrittlement and premature failure under service conditions. This weakness is primarily due to the absence of Cr, which severely limits oxidation resistance. Smith et al. [120] reported that adding > 2 wt% Cr or reducing Al below 0.2 wt% mitigates notch sensitivity, but Cr additions compromise low CTE, as shown in Fig. 14.

To resolve this trade-off, Incoloy 907 was introduced with Al reduced to ~0.1 wt% to minimise notch embrittlement, while Ti and Nb were increased to maintain strength. However, higher Ti promoted excessive  $\eta$ -phase precipitation during long-term ageing, reducing tensile strength compared to Incoloy 903. Further optimisation focused on Si additions, which significantly improved SAGBO resistance. As shown in Fig. 15, Si levels above 0.2 wt% enhanced stress-rupture life in smooth specimens, while >0.5 wt% shifted the fracture mode in notched specimens from notch failure to smooth-ligament failure. This improvement is attributed to Ni- and Nb-rich Laves phases forming along unrecrystallised grain boundaries, stabilising grain size under creep conditions [121]. Building on these findings, Incoloy 909 was developed. It retained the Ti-rich  $\gamma'$  strengthening mechanism while incorporating Si to improve tensile

strength, creep-rupture resistance, and eliminate notch sensitivity.

#### 4.4. Co–Cr balancing and Ni/Co optimisation

Although Incoloy 909 improved oxidation resistance compared to earlier alloys through reduced Al and added Si, its Cr-free design still offered only moderate oxidation resistance. To address this limitation, Sato et al. developed two new alloys, HRA929 and HRA929C (Table 3), to reintroduce Cr without compromising low thermal expansion or  $\gamma'$  phase stability [117]. The key strategy was to offset the CTE increase typically associated with Cr by partially substituting Ni with Co. When the combined Ni + Co content was fixed at 50 wt%, increasing the Co/(Co + Ni) ratio from 0.26 (Incoloy 909) to 0.40 (HRA929) reduced the CTE from  $7.69 \times 10^{-6} \text{ }^{\circ}\text{C}^{-1}$  to  $5.79 \times 10^{-6} \text{ }^{\circ}\text{C}^{-1}$  [117]. Co additions also promoted Laves phase precipitation, improving ductility and refining grain structure. Si additions further enhanced Laves phase formation, while a small amount of Al stabilised  $\gamma'$  during long-term ageing without inducing SAGBO, thereby improving creep resistance [122].

As shown in Fig. 16, HRA929 exhibits a lower CTE than both Incoloy 903 and 909 across the temperature range, owing to its higher Co content. Building on this, HRA929C incorporates an additional 2 wt% Cr, achieving oxidation resistance significantly superior to both Incoloy 909 and HRA929 while maintaining thermal expansion comparable to earlier alloys. Oxidation tests at 800 °C for 100 h revealed that the oxide scale on HRA929C was more than 70 % thinner than that on HRA929. Mechanical evaluations confirmed that HRA929C offers the highest high-temperature strength among the three alloys, while HRA929 falls between Incoloy 909 and HRA929C. Neither HRA929 nor HRA929C exhibited notch fracture during stress-rupture testing, in contrast to Incoloy 903, which failed under identical conditions. Post-ageing tests further showed superior yield strength retention for both alloys compared to Incoloy 909, indicating improved long-term stability [117].

Building on these principles, Wanner et al. [123] systematically investigated the effect of the Ni/Co ratio on CTE in controlled thermal expansion alloys. As shown in Fig. 17, when the combined Ni + Co content was fixed at ~50 wt% and 6.5 wt% Cr was added, the minimum CTE occurred at a Ni/Co ratio of ~0.5. These findings guided the development of THERMO-SPAN, a low-expansion alloy optimised for oxidation resistance and mechanical performance.

THERMO-SPAN demonstrated a significant improvement in oxidation resistance, with cyclic oxidation mass gain only one-sixth that of Incoloy 909. Mechanical testing revealed superior creep resistance and high-temperature tensile strength, while notch sensitivity remained as low as that of Incoloy 909, ensuring structural reliability under complex loading. In high-cycle thermal fatigue tests, THERMO-SPAN exhibited a markedly higher endurance limit than Incoloy 909 despite its slightly higher CTE [123]. This improvement is attributed to Al additions, which enhance  $\gamma'$  phase stability, and the combined influence of Al and Co aligns with earlier findings by Sato et al. [117]. The design strategy demonstrated by HRA929, HRA929C, and THERMO-SPAN involves using Co to counteract the CTE increase from Cr, while Cr mitigates SAGBO and enables Al additions without compromising notch

**Table 3**

Chemical compositions (wt%) of selected controlled thermal expansion alloy, with the balance being Fe.

Type	Ni	Co	Nb	Ti	Al	Si	B	Cr	Ref.
Incoloy 903	38.0	15	3.0	1.4	0.9	-	0.007	-	[117]
Incoloy 907	38.4	13	4.7	1.5	< 0.1	-	0.007	-	[117]
Incoloy 909	38.2	13	4.7	1.5	< 0.1	0.4	0.007	-	[117]
HRA929	29.2	19.6	4.02	1.29	0.55	0.45	0.004	-	[117]
HRA929C	29.5	22.5	4.07	1.3	0.54	0.31	0.004	2.03	[117]
THERMO-SPAN	24.5	29	4.8	0.8	0.45	0.35	0.004	5.5	[118]
Three phase alloy	33	31	3	0.6	5.3	-	-	-	[119]

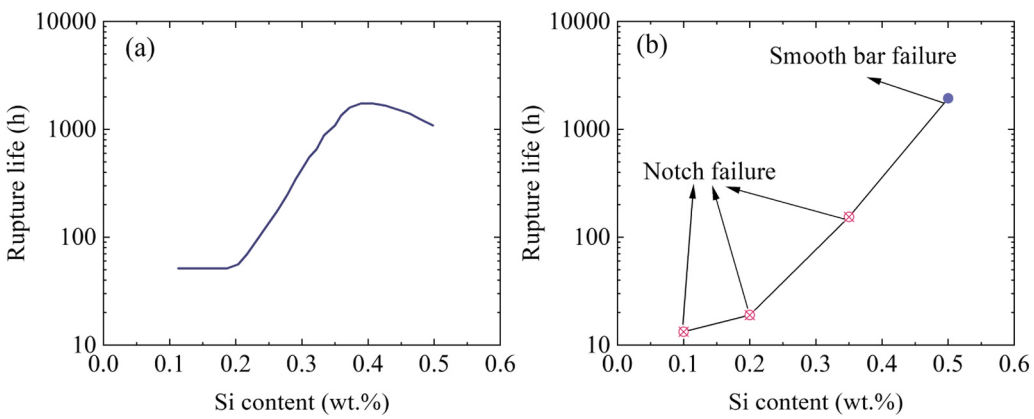


**Fig. 15.** Influence of Si content on stress-rupture properties of alloy specimens: (a) smooth bar and (b) notched bar ( $K_t = 2$ ), tested at 538 °C under 827.4 MPa, after [116].

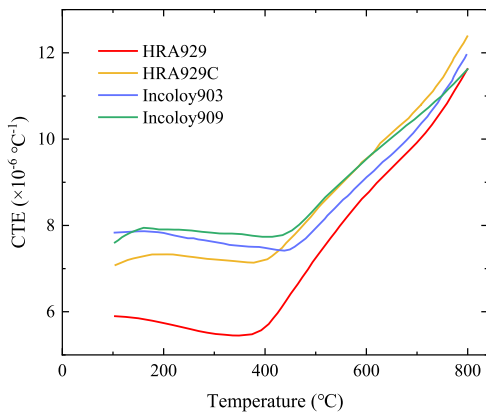


**Fig. 16.** CTE comparison among controlled thermal expansion alloys: HRA929, HRA929C, Incoloy 903, and Incoloy 909, after [117].

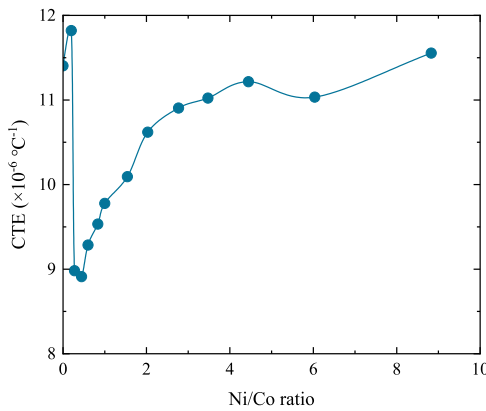


**Fig. 17.** Effect of Ni/Co ratio on the CTE at 510 °C for alloys with 50 wt% (Ni + Co) and 6.5 wt% Cr: CTE increases sharply up to 0.2 with (peak  $11.8 \times 10^{-6} \text{ }^{\circ}\text{C}^{-1}$ ), then decreases to a minimum of  $8.9 \times 10^{-6} \text{ }^{\circ}\text{C}^{-1}$  at 0.45, before increasing again, after [123].

resistance. This approach resolves the limitations of earlier alloys such as Incoloy 907 and 909, where Al was minimised to avoid SAGBO at the expense of  $\gamma'$  stability.

#### 4.5. An alternative path: High-Al three-phase ( $\gamma - \gamma' - \beta$ ) alloy

In contrast to the Co–Cr balanced design strategy, a fundamentally

different approach has been proposed to enhance oxidation resistance in controlled thermal expansion alloys. Heck et al. explored the effect of high Al content as an alternative means to improve the inherently limited oxidation resistance of Cr-free systems [124]. Alloys containing more than 5 wt% Al exhibited a marked change in fracture behaviour; as shown in Fig. 18(a), the fracture mode of notched specimens transitioned from notch failure to smooth-bar failure with increasing Al content. This transition is attributed to the formation of a body-centred tetragonal (BCT)  $\beta$  phase at elevated Al levels, which significantly improves oxidation resistance.

Building on this observation, a three-phase  $\gamma - \gamma' - \beta$  alloy was developed through Ni/Co ratio optimisation combined with controlled Ti and Nb additions to maintain ductility. Dilatometry results in Fig. 18 (b) show that the high Co content (31 wt%) in this alloy raises the  $T_c$  to 533 °C, exceeding that of Incoloy 909. However, the combined effect of high Al and adjusted Ni content results in a CTE in the ferromagnetic state that is over 25 % higher than that of Incoloy 909; in the paramagnetic state, the difference narrows to about 10 %. Despite this increase, the CTE remains lower than that of Inconel 718. Most notably, the high Al content provides a substantial improvement in oxidation resistance, as demonstrated by cyclic oxidation tests in Fig. 18(c), where the three-phase alloy outperforms Incoloy 909.

#### 4.6. Inflection temperatures and CTE benchmarks

All Invar-type controlled thermal expansion alloys exhibit a sharp change in CTE near the  $T_c$ , creating a thermal “inflection point.” Table 4 summarises the inflection points and corresponding CTE values in both ferromagnetic and paramagnetic states. These alloys maintain significantly lower CTE than ferritic steels, particularly below  $T_c$ . For reference, P91 ferritic steel has a CTE of  $11.6 \times 10^{-6} \text{ }^{\circ}\text{C}^{-1}$  at 300 °C and  $12.5 \times 10^{-6} \text{ }^{\circ}\text{C}^{-1}$  at 600 °C.

These comparisons highlight the effectiveness of composition tailoring to exploit the Invar effect and achieve substantial CTE reduction in austenitic alloys. However, excessively low CTE can cause thermal mismatch with ferritic components in power plant assemblies, leading to stress concentrations at joints and reduced service life. Furthermore, these alloys require high Ni content and often significant Co additions, which increase cost and limit their widespread use to specialised applications such as aerospace fasteners and turbine components.

#### 4.7. Design guidance for power-plant austenitics

Insights from the development of controlled thermal expansion alloys suggest that moderate Cr additions should not be excessively restricted when designing austenitic steels for power plant applications.

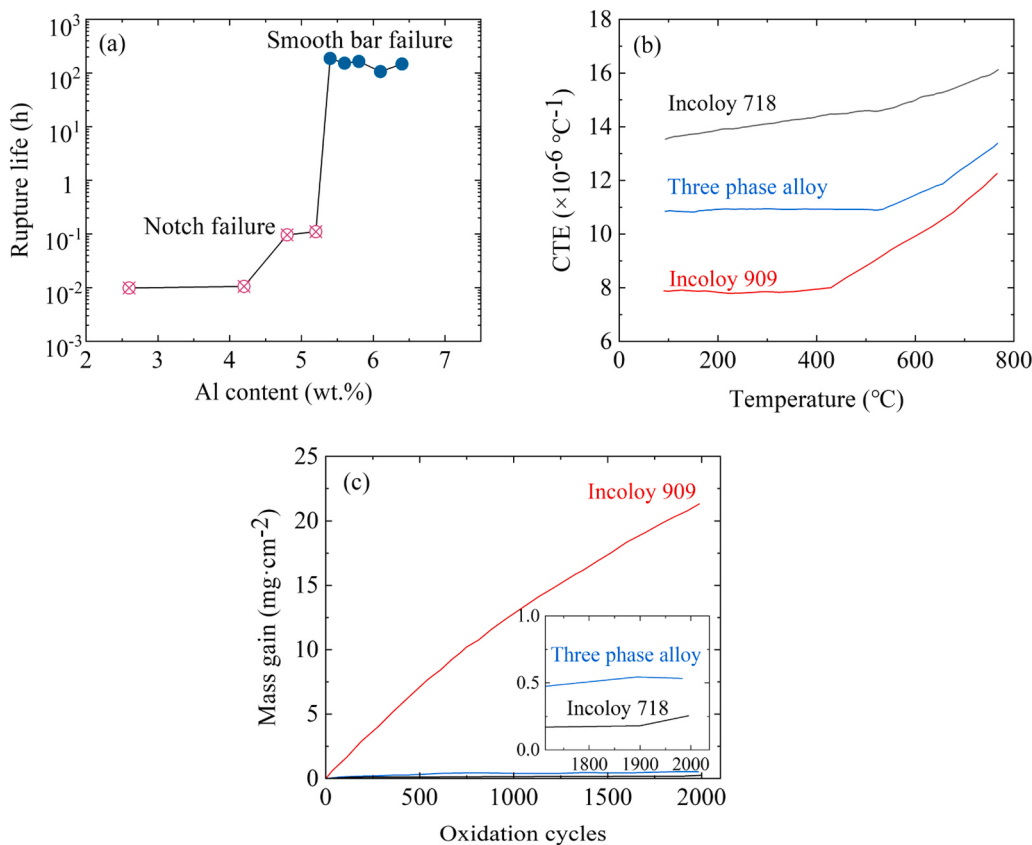


**Fig. 18.** (a) Effect of Al on notch sensitivity; (b) comparison of CTE; and (c) oxidation resistance among Inconel 718, the three-phase alloy, and Incoloy 909, after [124].

**Table 4**  
Inflection points and CTE in both ferromagnetic and paramagnetic states for different controlled thermal expansion alloys.

Alloy type	Inflection point ( $^{\circ}\text{C}$ )	CTE at $300^{\circ}\text{C}$ ( $\times 10^{-6}$ $^{\circ}\text{C}^{-1}$ )	CTE at $600^{\circ}\text{C}$ ( $\times 10^{-6}$ $^{\circ}\text{C}^{-1}$ )	Ref.
Incoloy 903	438	7.6	9.1	[117]
Incoloy 907	430	7.5	9.6	[117]
Incoloy 909	429	7.9	9.6	[117]
HRA929	354	5.4	8.7	[117]
HRA929C	385	7.2	9.5	[117]
THERMO-SPAN	321	8.2	12.2( $650^{\circ}\text{C}$ )	[118]
Three phase alloy	533	10.8	11.4	[119]

Below  $T_c$ , Cr slightly increases CTE, which can improve compatibility with ferritic steels while enhancing oxidation and corrosion resistance, critical for harsh operating environments. Conversely, Co content should be minimised to the level necessary for tuning  $T_c$ , preserving cost advantages over Ni-based superalloys.

Evidence supporting this approach comes from Oinuma et al., who optimised Ni and Cr levels in A286 for power plant application [125]. Their goal was to reduce thermal expansion while improving high-temperature mechanical properties. As shown in Fig. 19(a), increasing Ni and reducing Cr raised  $T_c$  (inflection point) and significantly lowered CTE at both  $100^{\circ}\text{C}$  (ferromagnetic state) and  $700^{\circ}\text{C}$  (paramagnetic state). The optimised composition, 40 wt% Ni and 6 wt% Cr, reduced CTE from  $16.3 \times 10^{-6} \text{ }^{\circ}\text{C}^{-1}$  (original A286) to  $10.4 \times 10^{-6} \text{ }^{\circ}\text{C}^{-1}$ , even lower than that of CrMoV ferritic steel, Fig. 19(b).

In addition to improved thermal stability, the modified alloy exhibited superior creep resistance and high-temperature tensile

strength compared to the original A286. Although its oxidation resistance was slightly lower than the baseline A286, it remained significantly superior to that of 12Cr ferritic steels, demonstrating the feasibility of this design strategy for advanced power plant components.

## 5. Conclusions and perspectives

### 5.1. Conclusions

Austenitic steels and Fe–Ni alloys provide an attractive compromise between cost and high-temperature performance compared to ferritic steels and Ni-based superalloys. However, their relatively high CTE remains a critical limitation, promoting thermal fatigue and residual stress at dissimilar joints. Reducing CTE is therefore a highly effective strategy for improving thermal fatigue resistance while preserving mechanical strength for thick-walled components in advanced power plants.

The CTE of Fe–Ni–Cr alloys is strongly composition-dependent: Fe and Cr tend to increase CTE, while Ni reduces it. Secondary phases, particularly  $\gamma'$ , also play a significant role due to their low CTE and substantial volume fraction. Increasing  $\gamma'$  fraction can therefore lower overall CTE, whereas other precipitates have a negligible influence. Despite these insights, no universally accurate predictive model for alloy CTE currently exists.

Exploiting the Invar effect offers a powerful route to achieving intrinsically low CTE. However, controlled thermal expansion alloys designed on this principle face persistent challenges: low  $T_c$ , oxidation susceptibility, and high cost due to Co additions. Furthermore, excessively low CTE can induce thermal mismatch with ferritic steels, reducing structural reliability. Future alloy design should adopt a multi-stage optimisation framework:

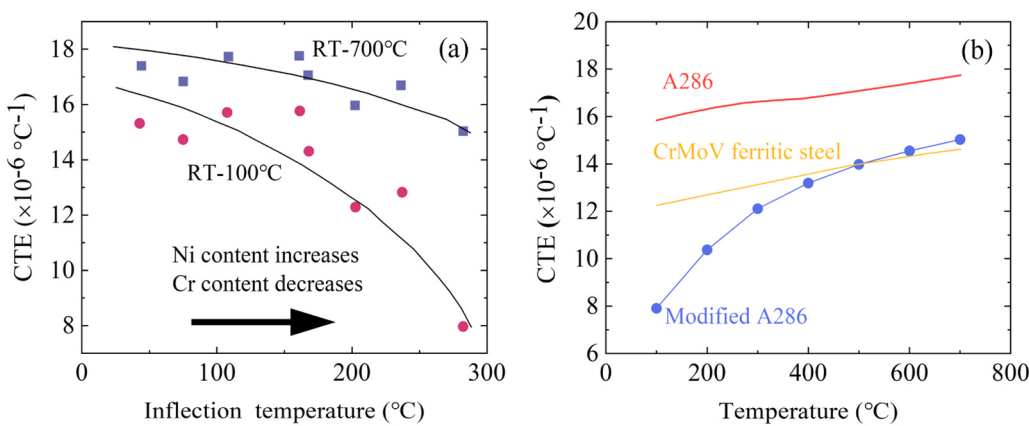


**Fig. 19.** (a) Relationship between magnetic transition temperature and mean CTE of austenitic steels, (b) The variation of CTE with temperature for A286 steel, CrMoV ferritic steel, and modified A286 steel, after [125].

- Ferromagnetic stage: Tailor Fe–Ni–Cr composition to activate the Invar effect.
- Inflection-point stage: Adjust Co and minor elements to extend the effective temperature range of the Invar effect.
- Paramagnetic stage: Apply conventional alloying and precipitation strategies to stabilise CTE and mechanical properties.

Emerging concepts such as Co–Cr balancing, Ni/Co ratio optimisation (e.g., THERMO-SPAN), and high-Al three-phase  $\gamma$ – $\gamma'$ – $\beta$  alloys demonstrate promising pathways to reconcile low CTE with oxidation resistance and creep strength.

## 5.2. Perspectives

Looking ahead, integrating computational thermodynamics with machine learning offers a transformative approach for multi-objective optimisation, enabling simultaneous control of CTE, creep resistance, oxidation behaviour, and cost. Such strategies will be pivotal in developing next-generation austenitic steels for USC and A-USC power plants, ensuring both thermal reliability and economic viability.

Capturing the complex, nonlinear relationships linking processing, microstructure, and properties remains challenging for traditional modelling. Leveraging expanding experimental and computational data sets, machine learning now enables accurate alloy property prediction and composition optimisation [126–130]. Multi-objective optimisation further enables the concurrent enhancement of multiple performance indicators, achieving a balance among thermal expansion control, mechanical strength, and cost [131–134].

It should be noted that for controlled thermal expansion alloys leveraging the Invar effect, experimental CTE data in the ferromagnetic stage (below the  $T_c$ ) are extremely limited, making it difficult to directly train machine learning models for this temperature range. Nevertheless, based on the literature reviewed, clear compositional guidelines have been established for activating the Invar effect and increasing the  $T_c$ , thereby extending its effective temperature range. In contrast, abundant datasets are available for the paramagnetic stage (above the  $T_c$ ), including alloy compositions, CTEs, and mechanical properties, provide a solid foundation for data-driven exploration and model development. By integrating these compositional guidelines with extensive high-temperature data sets, multi-objective optimisation can be employed to design austenitic alloys that simultaneously achieve controlled thermal expansion and superior high-temperature mechanical performance [135].

Moreover, integrating machine learning with computational thermodynamics helps overcome the limited predictive capability and poor generalisation of CALPHAD models across different alloy systems [136]. By embedding thermodynamic constraints into machine learning,

training datasets can be expanded, unphysical predictions avoided, and the interpretability of results enhanced, establishing a physically grounded foundation for alloy design [137–140]. Therefore, integrating machine learning for property prediction and multi-objective optimisation with computational thermodynamics offers a powerful and physically grounded framework for designing austenitic alloys with controlled thermal expansion suitable for USC and A-USC power plant applications.

## CRediT authorship contribution statement

**Yian Lin:** Writing – original draft, Validation, Software, Methodology, Investigation, Funding acquisition, Data curation. **Pengxin Wang:** Writing – original draft, Validation, Software, Data curation, Conceptualization. **Gebril M. A. M. El-Fallah :** Writing – review & editing, Writing – original draft, Visualization, Validation, Supervision, Methodology, Investigation, Formal analysis, Conceptualization.

## Declaration of Competing Interest

The authors declare that they have no known competing financial interests or personal relationships that could have influenced the work reported in this study.

## Acknowledgements

All authors gratefully acknowledge the support from the University of Leicester, particularly for providing a PhD scholarship for this study.

## Data availability

Data will be made available on request.

## References

- [1] J. Bugge, S. Kjær, R. Blum, High-efficiency coal-fired power plants development and perspectives, Energy 31 (2006) 1437–1445, <https://doi.org/10.1016/j.energy.2005.05.025>.
- [2] Q. Wang, J. Hong, Development of new pipes for ultra supercritical power station boilers, Baosteel Technol. 5 (2008) 44–53.
- [3] J. Patil, M. Palwal, S. Mishra, A review on the material development and corresponding properties for power plant applications, Mater. Perform. Charact. 11 (2022) 20200173, <https://doi.org/10.1520/MPC20200173>.
- [4] R. Blum, R. Vanstone, C. Messlier-Gouze, Materials development for boilers and steam turbines operating at 700 °C, in: 4th EPRI International Conference on Advanced in Material Technology for Fossil Power Plants, 2003, pp. 118–138.
- [5] S. Lee, et al., Comprehensive technical review of the high-efficiency low-emission technology in advanced coal-fired power plants, Rev. Chem. Eng. 39 (2021), <https://doi.org/10.1515/reve-2020-0107>.

- [6] C. Zhang, Z. Wang, Comprehensive energy efficiency analysis of ultra-supercritical thermal power units, *Appl. Therm. Eng.* 235 (2023) 121365, <https://doi.org/10.1016/j.applthermeng.2023.121365>.
- [7] K. Kubushiro, et al., Development of boiler technology for 700C A-USC plant, *IHI Eng. Rev.* 49 (2016) 34–43.
- [8] P.J. Ennis, Ferritic and martensitic steels for power plants, in: *Structural Alloys for Power Plants*, Elsevier, 2014, pp. 188–220.
- [9] R.L. Klueh, Elevated temperature ferritic and martensitic steels and their application to future nuclear reactors, *Int. Mater. Rev.* 50 (2005) 287–310, <https://doi.org/10.1179/174328005X41140>.
- [10] L. Leibowitz, R.A. Blomquist, Thermal conductivity and thermal expansion of stainless steels D9 and HT9, *Int. J. Thermophys.* 9 (1988) 873–883, <https://doi.org/10.1007/BF00503252>.
- [11] F. Masuyama, et al., Findings on creep-fatigue damage in pressure parts of long-term service-exposed thermal power plants, *J. Press. Vessel Technol.* 107 (1985) 260–270, <https://doi.org/10.1115/1.3264447>.
- [12] J.Y. Park, et al., Fatigue behaviors of high nitrogen stainless steels with different deformation modes, *Mater. Sci. Eng.: A* 682 (2017) 622–628, <https://doi.org/10.1016/j.msea.2016.11.053>.
- [13] A. Järvenpää, L.P. Karjalainen, M. Jaskari, Effect of grain size on fatigue behavior of Type 301LN stainless steel, *Int. J. Fatigue* 65 (2014) 93–98, <https://doi.org/10.1016/j.ijfatigue.2013.05.012>.
- [14] Y.-J. Oh, et al., Thermomechanical fatigue behavior and lifetime prediction of niobium-bearing ferritic stainless steels, *Int. J. Fatigue* 40 (2012) 36–42, <https://doi.org/10.1016/j.ijfatigue.2012.01.013>.
- [15] A. Di Gianfrancesco, 1 – the fossil fuel power plants technology, in: A. Di Gianfrancesco (Ed.), *Materials for Ultra-Supercritical and Advanced Ultra-Supercritical Power Plants*, Woodhead Publishing, 2017, pp. 1–49.
- [16] A. Shibli, F. Starr, Some aspects of plant and research experience in the use of new high strength martensitic steel P91, *Int. J. Press. Vessels Pip.* 84 (2007) 114–122, <https://doi.org/10.1016/j.ijpvp.2006.11.002>.
- [17] J. Hald, Metallurgy and creep properties of new 9–12 % Cr steels, *Steel Res.* 67 (1996) 369–374, <https://doi.org/10.1002/srin.199605503>.
- [18] S. Swaminathan, et al., Evolution of surface chemistry and morphology of oxide scale formed during initial stage oxidation of modified 9Cr–1Mo steel, *Corros. Sci.* 79 (2014) 59–68, <https://doi.org/10.1016/j.corsci.2013.10.026>.
- [19] M. Schütze, et al., The role of alloy composition, environment and stresses for the oxidation resistance of modern 9% Cr steels for fossil power stations, *Mater. Res.* 7 (2004) 111–123.
- [20] K. Yin, et al., Corrosion behavior of ferritic/martensitic steel P92 in supercritical water, *J. Supercrit. Fluids* 50 (2009) 235–239, <https://doi.org/10.1016/j.supflu.2009.06.019>.
- [21] L. Tan, X. Ren, T.R. Allen, Corrosion behavior of 9–12 % Cr ferritic–martensitic steels in supercritical water, *Corros. Sci.* 52 (2010) 1520–1528, <https://doi.org/10.1016/j.corsci.2009.12.032>.
- [22] V. Shankar, et al., Low cycle fatigue behavior and microstructural evolution of modified 9Cr–1Mo ferritic steel, *Mater. Sci. Eng.: A* 437 (2006) 413–422, <https://doi.org/10.1016/j.msea.2006.07.146>.
- [23] Y. Zhao, et al., An overview on the novel heat-resistant ferritic stainless steels, *Tungsten* 5 (2023) 467–480, <https://doi.org/10.1007/s42864-022-00171-4>.
- [24] R. Viswanathan, et al., U.S. program on materials technology for ultra-supercritical coal power plants, *J. Mater. Eng. Perform.* 14 (2005) 281–292, <https://doi.org/10.1361/10599490524039>.
- [25] H.K.D.H. Bhadeshia, Diffusion of carbon in austenite, *Met. Sci.* 15A (1981) 477–480, <https://doi.org/10.1179/03634581790426525>.
- [26] J. Weertman, Steady-state creep through dislocation climb, *J. Appl. Phys.* 28 (1957) 362–364, <https://doi.org/10.1063/1.1722747>.
- [27] H. Magnusson, R. Sandström, The role of dislocation climb across particles at creep conditions in 9–12 pct Cr steels, *Metall. Mater. Trans. A* 38 (2007) 2428–2434, <https://doi.org/10.1007/s11661-007-9280-9>.
- [28] R. Oruganti, M. Karadge, S. Swaminathan, Damage mechanics-based creep model for 9–10 %Cr ferritic steels, *Acta Mater.* 59 (2011) 2145–2155, <https://doi.org/10.1016/j.actamat.2010.12.015>.
- [29] H. Zhao, et al., Effect of long-term thermal aging on microstructure evolution and creep deformation behavior of a novel 11Cr–3W–3Co martensite ferritic steel, *Materials* 15 (2022) 3659, <https://doi.org/10.3390/ma15103659>.
- [30] K. Sawada, K. Kubo, F. Abe, Contribution of coarsening of MX carbonitrides to creep strength degradation in high chromium ferritic steel, *Mater. Sci. Technol.* 19 (2003) 732–738, <https://doi.org/10.1179/026708303225010687>.
- [31] M. Godec, D.A. Skobir Balantić, Coarsening behaviour of M23C6 carbides in creep-resistant steel exposed to high temperatures, *Sci. Rep.* 6 (2016) 29734, <https://doi.org/10.1038/srep29734>.
- [32] A. Strang, V. Vodarek, Z phase formation in martensitic 12CrMoVNb steel, *Mater. Sci. Technol.* 12 (1996) 552–556, <https://doi.org/10.1179/mst.1996.12.7.552>.
- [33] J.P.T. Vossen, et al., Limits of the oxidation resistance of several heat-resistant steels under isothermal and cyclic oxidation as well as under creep in air at 650 °C, *Mater. High Temp.* 14 (1997) 387–401, <https://doi.org/10.1080/09603409.1997.11689565>.
- [34] K. SUZUKI, et al., Precipitation of Z-phase and precipitation sequence during creep deformation of mod. 9Cr–1Mo steel, *Tetsu-to-Hagane* 89 (2003) 691–698, <https://doi.org/10.2355/tetsutohagane1955.89.6.691>.
- [35] K. Sawada, H. Kushima, K. Kimura, Z-phase formation during creep and aging in 9–12% Cr heat resistant steels, *ISIJ Int.* 46 (2006) 769–775, <https://doi.org/10.2355/isijinternational.46.769>.
- [36] Y. Kang, et al., Effect of Ti content on grain size and mechanical properties of UNS S44100 ferritic stainless steel, *Mater. Sci. Eng.: A* 677 (2016) 211–221, <https://doi.org/10.1016/j.msea.2016.08.070>.
- [37] V. Thomas Paul, S. Saroja, M. Vijayalakshmi, Microstructural stability of modified 9Cr–1Mo steel during long term exposures at elevated temperatures, *J. Nucl. Mater.* 378 (2008) 273–281, <https://doi.org/10.1016/j.jnucmat.2008.06.033>.
- [38] F. Abe, Creep rates and strengthening mechanisms in tungsten-strengthened 9Cr steels, *Mater. Sci. Eng.: A* 319–321 (2001) 770–773, [https://doi.org/10.1016/S0921-5093\(00\)02002-5](https://doi.org/10.1016/S0921-5093(00)02002-5).
- [39] Y. Toda, et al., Effects of W and Co on long-term creep strength of precipitation strengthened 15Cr ferritic heat resistant steels, *ISIJ Int.* 43 (2003) 112–118, <https://doi.org/10.2355/isijinternational.43.112>.
- [40] R.L. Klueh, A.T. Nelson, Ferritic/martensitic steels for next-generation reactors, *J. Nucl. Mater.* 371 (2007) 37–52, <https://doi.org/10.1016/j.jnucmat.2007.05.005>.
- [41] G.M.A.M. El-Fallah, S.W. Ooi, H.K.D.H. Bhadeshia, Effect of nickel aluminide on the bainite transformation in a Fe–0.45C–13Ni–3Al–4Co steel, and associated properties, *Mater. Sci. Eng.: A* 767 (2019) 138362, <https://doi.org/10.1016/j.msea.2019.138362>.
- [42] G.M.A.M. El-Fallah, H.K.D.H. Bhadeshia, Tensile behaviour of thermally-stable nanocrystalline bainitic-steels, *Mater. Sci. Eng.: A* 746 (2019) 145–153, <https://doi.org/10.1016/j.msea.2018.12.124>.
- [43] Y. Toda, et al., Improvement in creep strength of precipitation strengthened 15Cr ferritic steel by controlling carbon and nitrogen contents, *JSME Int. J. Ser. A Solid Mech. Mater. Eng.* 48 (2005) 35–40, <https://doi.org/10.1299/jsmea.48.35>.
- [44] F. Abe, Precipitate design for creep strengthening of 9% Cr tempered martensitic steel for ultra-supercritical power plants, *Sci. Technol. Adv. Mater.* 9 (2008) 013002, <https://doi.org/10.1088/1468-6996/9/1/013002>.
- [45] K. Sawada, et al., Effect of tempering temperature on Z-phase formation and creep strength in 9Cr–1Mo–V–Nb–N steel, *Mater. Sci. Eng.: A* 480 (2008) 558–563, <https://doi.org/10.1016/j.msea.2007.09.031>.
- [46] H. Wang, et al., Precipitation and properties at elevated temperature in austenitic heat-resistant steels—a review, *Steel Res. Int.* 92 (2021) 2000378, <https://doi.org/10.1002/srin.202000378>.
- [47] H.K.D.H. Bhadeshia, R.W.K. Honeycombe, *Steels: Structure, Properties, and Design*, Elsevier, 2024.
- [48] F. Masuyama, History of power plants and progress in heat resistant steels, *ISIJ Int.* 41 (6) (2001) 612, <https://doi.org/10.2355/isijinternational.41.612>.
- [49] T. Sourmail, Precipitation in creep resistant austenitic stainless steels, *Mater. Sci. Technol.* 17 (2001) 1–14, <https://doi.org/10.1179/026708301101508972>.
- [50] T.L. Bergman, *Fundamentals of Heat and Mass Transfer*, John Wiley & Sons, 2011.
- [51] P.D. Jablonski, D.E. Alman, Oxidation resistance and mechanical properties of experimental low coefficient of thermal expansion (CTE) Ni-base alloys, *Int. J. Hydrom. Energy* 32 (2007) 3705–3712, <https://doi.org/10.1016/j.ijhydene.2006.08.019>.
- [52] J. Shingledecker, R. Purgett, P. Rawls, Current status of the U.S. DOE/OCDO A-USC materials technology research and development program, in: AM-EPRI 2013, 2013.
- [53] F. Masuyama, Alloy development and material issues with increasing steam temperature, in: AM-EPRI 2004, 2004.
- [54] T. Saju, M. Velu, Review on welding and fracture of nickel based superalloys, *Mater. Today: Proc.* 46 (2021) 7161–7169, <https://doi.org/10.1016/j.mpr.2020.11.334>.
- [55] F. Abe, T.-U. Kern, R. Viswanathan, in: *Structural Alloys for Power Plants*, Elsevier, 2008 (Ed.).
- [56] G. Mitra, S. Mitra, Grüneisen's rule and the thermal expansion of metals, *Nature* 179 (1957) 1295–1296.
- [57] Y. Yin, R. Faulkner, F. Starr, Austenitic steels and alloys for power plants, in: (Ed.), 2014, pp. 105–52.
- [58] R. Zhou, L. Zhu, Growth behavior and strengthening mechanism of Cu-rich particles in sanciro 25 austenitic heat-resistant steel after aging at 973 K, *Mater. Sci. Eng.: A* 796 (2020) 139973, <https://doi.org/10.1016/j.msea.2020.139973>.
- [59] F.C. Hull, et al., Effect of composition on thermal expansion of alloys used in power generation, *J. Mater. Eng.* 9 (1987) 81–92, <https://doi.org/10.1007/BF02833790>.
- [60] Y. Wu, X. Qin, L. Zhou, Effects of alloying elements on thermal expansion behavior of Ni–Fe–Cr-based superalloys, *Metall. Mater. Trans. A* 49 (2018) 5653–5660, <https://doi.org/10.1007/s11661-018-4898-3>.
- [61] R. Yamamoto, et al., Development and trial manufacturing of Ni-based superalloy “LTES700R” for advanced 700C class steam turbines, in: AM-EPRI 2013, 2013.
- [62] P.K. Sung, D.R. Poirier, Estimation of densities and coefficients of thermal expansion of solid Ni-base superalloys, *Mater. Sci. Eng.: A* 245 (1998) 135–141, [https://doi.org/10.1016/S0921-5093\(97\)00699-0](https://doi.org/10.1016/S0921-5093(97)00699-0).
- [63] N. Dong, et al., The effects of Co and W on structural stability and mechanical properties of austenitic heat-resistant steel Sanciro 25: a first-principle study, *Metals* 10 (2020), <https://doi.org/10.3390/met10081051>.
- [64] H. Morrow, D.L. Sponseller, M. Semchyshen, The effects of molybdenum and aluminum on the thermal expansion coefficients of nickel-base alloys, *Metall. Trans. A* 6 (1975) 477, <https://doi.org/10.1007/BF02658405>.
- [65] D.R. Muzyka, C.R. Whitney, D.K. Schlosser, Physical metallurgy and properties of a new controlled-expansion superalloy, *JOM* 27 (1975) 11–15, <https://doi.org/10.1007/BF03355928>.
- [66] T. Ohno, et al., Development of low thermal expansion nickel base superalloy for steam turbine applications, *Energy Mater.* 2 (2007) 222–226.

- [67] M.V. Nathal, R.A. Mackay, R.G. Garlick, Temperature dependence of  $\gamma$ - $\gamma'$  lattice mismatch in Nickel-base superalloys, Mater. Sci. Eng. 75 (1985) 195–205, [https://doi.org/10.1016/0025-5416\(85\)90189-2](https://doi.org/10.1016/0025-5416(85)90189-2).
- [68] R.M. Levy, Principles of Solid State Physics, Elsevier, 2012.
- [69] S. Hwang, F. Hull, J. Wells, Effects of the alloying elements on the thermal expansion coefficient of nonmagnetic Ni-base alloys and austenitic steels, in: Fifth International Symposium on Superalloys, Seven Springs (PA), USA, 1984.
- [70] Z. Yan, et al., Phase evolution and thermal expansion behavior of a  $\gamma'$  precipitated Ni-based superalloy by synchrotron X-ray diffraction, Acta Metall. Sin. (Engl. Lett.) 35 (2022) 93–102, <https://doi.org/10.1007/s40195-021-01321-2>.
- [71] M.S.A. Karunaratne, et al., Modelling the coefficient of thermal expansion in Ni-based superalloys and bond coatings, J. Mater. Sci. 51 (2016) 4213–4226, <https://doi.org/10.1007/s10853-015-9554-3>.
- [72] S. Raju, et al., Thermal expansion studies on Inconel-600® by high temperature X-ray diffraction, J. Nucl. Mater. 325 (2004) 18–25, <https://doi.org/10.1016/j.jnucmat.2003.10.007>.
- [73] G. Bruno, et al., Measurement of the lattice misfit of the nickel-base superalloy SC16 by high-energy synchrotron radiation, Metall. Mater. Trans. A 34 (2003) 193–197, <https://doi.org/10.1007/s11661-003-0321-8>.
- [74] Y. Wang, Z.K. Liu, L.Q. Chen, Thermodynamic properties of Al, Ni, NiAl, and Ni<sub>3</sub>Al from first-principles calculations, Acta Mater. 52 (2004) 2665–2671, <https://doi.org/10.1016/j.actamat.2004.02.014>.
- [75] Y.N. Gornostyrev, et al., The role of thermal expansion and composition changes in the temperature dependence of the lattice misfit in two-phase  $\gamma$ - $\gamma'$  superalloys, Scr. Mater. 56 (2007) 81–84, <https://doi.org/10.1016/j.scriptamat.2006.10.002>.
- [76] D. Kim, S.-L. Shang, Z.-K. Liu, Effects of alloying elements on thermal expansions of  $\gamma$ -Ni and  $\gamma$ -Ni<sub>3</sub>Al by first-principles calculations, Acta Mater. 60 (2012) 1846–1856, <https://doi.org/10.1016/j.actamat.2011.12.005>.
- [77] S. Cheng, et al., Effects of Al and Ti on thermal expansion behavior of a Ni-Fe-Cr-based superalloy: a combined experimental and first-principle study, J. Mater. Res. Technol. 29 (2024) 3805–3812, <https://doi.org/10.1016/j.jmrt.2024.02.080>.
- [78] E. Salama, M.M. Eissa, A.S. Tageldin, Distinct properties of tungsten austenitic stainless alloy as a potential nuclear engineering material, Nucl. Eng. Technol. 51 (2019) 784–791, <https://doi.org/10.1016/j.net.2018.12.021>.
- [79] Q.-H. Hu, et al., Effect of Mo on the  $\sigma$ -phase precipitation behavior of super-austenitic stainless steel, Emerg. Mater. Res. 13 (2024) 141–151, <https://doi.org/10.1680/jemmr.23.00085>.
- [80] H.-P. Ebert, S. Braxmeier, D. Neubert, Intercomparison of Thermophysical Property Measurements on Iron and Steels, Int. J. Thermophys. 40 (2019) 96, <https://doi.org/10.1007/s10765-019-2568-3>.
- [81] Y.S. Touloukian, Thermophysical properties of matter, in: The TPRC Data Series, 1972.
- [82] C.-É. Guillaume, Recherches sur les aciers au nickel, J. Phys. Theor. Appl. 7 (1898) 262–274, <https://doi.org/10.1051/jphystap:018980070026200>.
- [83] A. Sahoo, V.R.R. Medicherla, Fe-Ni Invar alloys: a review, Mater. Today: Proc. 43 (2021) 2242–2244, <https://doi.org/10.1016/j.matr.2020.12.527>.
- [84] R.J. Weiss, The origin of the 'Invar' effect, Proc. Phys. Soc. 82 (1963) 281–288, <https://doi.org/10.1088/0370-1328/82/2/314>.
- [85] C.-D. Kim, M. Matsui, S. Chikazumi, Magnetostriction of Fe-Ni Invar alloys, J. Phys. Soc. Jpn. 44 (1978) 1152–1157.
- [86] S. Chikazumi, et al., The invar problem, J. Appl. Phys. 39 (1968) 939–944, <https://doi.org/10.1063/1.1656337>.
- [87] M. van Schilfgaarde, I.A. Abrikosov, B. Johansson, Origin of the Invar effect in iron-nickel alloys, Nature 400 (1999) 46–49, <https://doi.org/10.1038/21848>.
- [88] D. Roy, D. Pettifor, Stoner theory support for the two-state hypothesis for  $\gamma$  iron, J. Phys. F: Met. Phys. 7 (1977) L183, <https://doi.org/10.1088/0305-4608/7/7/004>.
- [89] H.K. Bhadeshia, Theory of Transformations in Steels, CRC Press, 2021.
- [90] L. Kaufman, E.V. Clougherty, R.J. Weiss, The lattice stability of metals—III. Iron, Acta Metall. 11 (1963) 323–335, [https://doi.org/10.1016/0001-6160\(63\)90157-3](https://doi.org/10.1016/0001-6160(63)90157-3).
- [91] L. Kaufman, Condensed state reactions at high pressure, 1965.
- [92] W. S. Owen, The influence of lattice softening of the parent phase on the martensitic transformation in Fe-Ni and Fe-Pt alloys, Mater. Sci. Eng.: A 127 (1990) 197–204, [https://doi.org/10.1016/0921-5093\(90\)90310-Y](https://doi.org/10.1016/0921-5093(90)90310-Y).
- [93] M. Matsui, K. Adachi, Magneto-elastic properties and invar anomaly of Fe-Pd alloys, Phys. B: Condens. Matter 161 (1990) 53–59, [https://doi.org/10.1016/0921-4526\(89\)90102-6](https://doi.org/10.1016/0921-4526(89)90102-6).
- [94] M. Inaba, et al., Development of an Invar (Fe-36Ni) shadow mask for color cathode ray tubes, IEEE Trans. Electron Devices 35 (1988) 1721–1729, <https://doi.org/10.1109/16.7378>.
- [95] M. Shiga, Invar alloys, Curr. Opin. Solid State Mater. Sci. 1 (1996) 340–348, [https://doi.org/10.1016/S1359-0286\(96\)80023-4](https://doi.org/10.1016/S1359-0286(96)80023-4).
- [96] S. Jacobs, Dimensional stability of materials useful in optical engineering, Opt. Acta 33 (1986) 1377–1388, <https://doi.org/10.1080/713821886>.
- [97] C. Chen, et al., Refinement mechanism and physical properties of arc melted invar alloy with different modifiers, Mater. Chem. Phys. 227 (2019) 138–147, <https://doi.org/10.1016/j.matchemphys.2019.02.006>.
- [98] H. Asgari, et al., On thermal expansion behavior of invar alloy fabricated by modulated laser powder bed fusion, Mater. Des. 160 (2018) 895–905, <https://doi.org/10.1016/j.matdes.2018.10.025>.
- [99] Q. Yang, et al., Microstructures and unique low thermal expansion of Invar 36 alloy fabricated by selective laser melting, Mater. Charact. 166 (2020) 110409, <https://doi.org/10.1016/j.matchar.2020.110409>.
- [100] M. Yakout, M.A. Elbestawi, S.C. Veldhuis, A study of thermal expansion coefficients and microstructure during selective laser melting of Invar 36 and stainless steel 316L, Addit. Manuf. 24 (2018) 405–418, <https://doi.org/10.1016/j.addma.2018.09.035>.
- [101] Q. Yang, et al., In-situ X-ray computed tomography of high-temperature tensile behavior for laser powder bed fused Invar 36 alloy, Addit. Manuf. 83 (2024) 104072, <https://doi.org/10.1016/j.addma.2024.104072>.
- [102] N.J. Harrison, I. Todd, K. Mumtaz, Thermal expansion coefficients in Invar processed by selective laser melting, J. Mater. Sci. 52 (2017) 10517–10525, <https://doi.org/10.1007/s10853-017-1169-4>.
- [103] Y. TANJI, Y. SHIRAKAWA, Thermal expansion coefficient of Fe-Ni FCC alloyS, J. Jpn. Inst. Met. 34 (1970) 228–232, <https://doi.org/10.2320/jinstmet1952.34.2.228>.
- [104] M. Kul, B. Akgul, Y.Z. Karabay, The relationship of hot and cold rolling processes with the structure and properties of invar 36, Mater. Chem. Phys. 295 (2023) 127215, <https://doi.org/10.1016/j.matchemphys.2022.127215>.
- [105] J.-F Zhang, et al., Effect of solid solution treatment on microstructure of Fe-Ni based high strength low thermal expansion alloy, J. Iron Steel Res. Int. 15 (2008) 75–78, [https://doi.org/10.1016/S1006-706X\(08\)60016-3](https://doi.org/10.1016/S1006-706X(08)60016-3).
- [106] T. Wakui, et al., Optimum temperature for HIP bonding Invar alloy and stainless steel, Mater. Trans. 60 (2019) 1026–1033, <https://doi.org/10.2320/matertrans.M2018346>.
- [107] K. Wei, et al., Planar lattices with tailororable coefficient of thermal expansion and high stiffness based on dual-material triangle unit, J. Mech. Phys. Solids 86 (2016) 173–191, <https://doi.org/10.1016/j.jmps.2015.10.004>.
- [108] H. Xu, A. Farag, D. Pasini, Routes to program thermal expansion in three-dimensional lattice metamaterials built from tetrahedral building blocks, J. Mech. Phys. Solids 117 (2018) 54–87, <https://doi.org/10.1016/j.jmps.2018.04.012>.
- [109] K. Wang, et al., Three-dimensional metamaterials based on discrete assembly to customize thermal expansion response under temperature stimuli, Appl. Mater. Today 41 (2024) 102460, <https://doi.org/10.1016/j.apmt.2024.102460>.
- [110] J.R. Davis, Nickel, Cobalt, and Their Alloys, ASM international, 2000.
- [111] N. Solov'eva, et al., Effect of ruthenium, rhodium, and palladium on the coefficient of thermal expansion of iron-nickel and iron-nickel-cobalt alloys, Met. Sci. Heat Treat. 10 (1968) 293–294, <https://doi.org/10.1007/BF00653113>.
- [112] T.K. Ha, S.H. Min, Effect of C content on the microstructure and physical properties of Fe-36Ni Invar alloy, Mater. Sci. Forum 804 (2015) 293–296, <https://doi.org/10.4028/www.scientific.net/MSF.804.293>.
- [113] M. Tsuda, Effect of minor alloying elements on the mean thermal expansion coefficient of Fe-36 % Ni invar alloy, Tetsu-to-Hagané 80 (1994) 944–949, <https://doi.org/10.2355/tetsutohagané1955.80.12.944>.
- [114] Y. Tanji, Y. Shirakawa, Thermal Expansion Coefficient of Fe-Ni (fcc) Alloys, Tohoku University, 1970.
- [115] J. Wang, et al., An in-situ high-throughput study of the Invar effect in the Fe-Ni-Co system, J. Alloy. Compd. 1010 (2025) 177755, <https://doi.org/10.1016/j.jallcom.2024.177755>.
- [116] E.A. Wanner, et al., The current status of controlled thermal expansion superalloys, JOM 43 (1991) 38–43, <https://doi.org/10.1007/BF03220162>.
- [117] K. Sato, T. Ohno, Development of low thermal expansion superalloy, J. Mater. Eng. Perform. 2 (1993) 511–516, <https://doi.org/10.1007/BF02661734>.
- [118] E. Wanner, Development of a new controlled thermal expansion superalloy with improved oxidation resistance, Superalloys 1992 (1992) 237–246.
- [119] K. Heck, et al., Three-phase Controlled Expansion Superalloys with Oxidation Resistance, TMS, 1992, pp. 217–226.
- [120] D. Smith, et al., Improving the notch-rupture strength of low-expansion superalloys, in: Proceedings of the 4th International Symposium on Superalloys, Anonymous ASM, Champion, PA, USA, 1980.
- [121] K. Heck, The effects of silicon and processing on the structure and properties of Incoloy alloy 909, Phys. Metall. Control. Expans. Invar-Type Alloy. (1989) 273–282.
- [122] Z. Chen, J. Brooks, M. Loretto, Precipitation in Incoloy alloy 909, Mater. Sci. Technol. 9 (1993) 647–653, <https://doi.org/10.1179/mst.1993.9.8.647>.
- [123] E.A. Wanner, D.A. DeAntonio, in: Development of a New Controlled Thermal Expansion Superalloy with Improved Oxidation Resistance, 1992 (ed.).
- [124] K.A. Heck, et al., Three-Phase Controlled Expansion Superalloys with Oxidation Resistance, Inco Alloys International, Huntington, WV, USA, 1992, pp. 217–226.
- [125] S. Oinuma, et al., Development of low thermal expansion Fe-Ni-Cr austenitic heat resistant steel for high temperature steam turbine, in: AM-EPRI 2016, 2016.
- [126] X. Hu, et al., Two-way design of alloys for advanced ultra supercritical plants based on machine learning, Comput. Mater. Sci. 155 (2018) 331–339, <https://doi.org/10.1016/j.commatsci.2018.09.003>.
- [127] L. He, et al., Fatigue life evaluation model for various austenitic stainless steels at elevated temperatures via alloy features-based machine learning approach, Fatigued Fract. Eng. Mater. Struct. 46 (2023) 699–714, <https://doi.org/10.1111/ffe.13895>.
- [128] J.-J. He, et al., Application of soft constrained machine learning algorithms for creep rupture prediction of an austenitic heat resistant steel Sanicro 25, J. Mater. Res. Technol. 22 (2023) 923–937, <https://doi.org/10.1016/j.jmrt.2022.11.154>.
- [129] P. Wang, G.M.A.M. El-Fallah, A Data-driven machine learning model for radiation-induced DBTT shifts in RAFM steels, J. Nucl. Mater. 615 (2025) 155984, <https://doi.org/10.1016/j.jnucmat.2025.155984>.
- [130] P. Wang, et al., Advanced machine learning analysis of radiation hardening in reduced-activation ferritic/martensitic steels, Comput. Mater. Sci. 251 (2025) 113773, <https://doi.org/10.1016/j.commatsci.2025.113773>.

- [131] X. Pengcheng, et al., Multi-objective optimization in machine learning assisted materials design and discovery, *J. Mater. Inform.* 5 (2025) 26, <https://doi.org/10.20517/jmi.2024.108>.
- [132] Y. Deng, et al., An intelligent design for Ni-based superalloy based on machine learning and multi-objective optimization, *Mater. Des.* 221 (2022) 110935, <https://doi.org/10.1016/j.matdes.2022.110935>.
- [133] Y. Zhu, et al., Designing nickel-based superalloys with high creep life and low thermal expansion coefficient using machine learning assisted by multi-objective optimization, *J. Mater. Sci.* 60 (2025) 9743–9757, <https://doi.org/10.1007/s10853-025-10872-z>.
- [134] J.L.J. Pereira, et al., A review of multi-objective optimization: methods and algorithms in mechanical engineering problems, *Arch. Comput. Methods Eng.* 29 (2022) 2285–2308, <https://doi.org/10.1007/s11831-021-09663-x>.
- [135] A. Suzuki, C. Shen, N. Chennimalai Kumar, Application of computational tools in alloy design, *MRS Bull.* 44 (2019) 247–251, <https://doi.org/10.1557/mrs.2019.70>.
- [136] C. Shen, The synergy of machine learning and CALPHAD: Revitalizing traditional approaches, *Comput. Mater. Sci.* 258 (2025) 113970, <https://doi.org/10.1016/j.commatsci.2025.113970>.
- [137] S.Y. Kwon, et al., Physics-coupled data-driven design of high-temperature alloys, *Acta Mater.* 284 (2025) 120622, <https://doi.org/10.1016/j.actamat.2024.120622>.
- [138] Z. Rao, et al., Machine learning-enabled high-entropy alloy discovery, *Science* 378 (2022) 78–85, <https://doi.org/10.1126/science.abo4940>.
- [139] W. Mu, et al., Predicting strain-induced martensite in austenitic steels by combining physical modelling and machine learning, *Mater. Des.* 197 (2021) 109199, <https://doi.org/10.1016/j.matdes.2020.109199>.
- [140] P. Wang, G.M.A.M. El-Fallah, Physically- and knowledge-informed deep learning for robust prediction of martensite start temperature in steels, *Mater. Today Commun.* 49 (2025) 113743, <https://doi.org/10.1016/j.mtcomm.2025.113743>.